RSC Advances

ROYAL SOCIETY OF CHEMISTRY

PAPER

View Article Online
View Journal | View Issue

Cite this: *RSC Adv.*, 2021, **11**, 16592

Preparation of rGO@Fe_3O_4 nanocomposite and its application to enhance the thermal conductivity of epoxy resin

Jiaqi Geng,[a] Yuanli Men,[a] Chen Liu,[a] Xiang Ge*[b] and Caideng Yuan *[a]

Received 22nd March 2021
Accepted 27th April 2021

DOI: 10.1039/d1ra02254g

rsc.li/rsc-advances

In this study, we report a simple method to improve the thermal conductivity of epoxy resin by using new magnetic composites as fillers. The rGO@Fe_3O_4 nanocomposite has been prepared by a solvothermal method, and its morphology and chemical structure were characterized and analyzed by various characterization methods. Afterwards, the rGO@Fe_3O_4/EP composite material was obtained in an external magnetic field, in which the rGO@Fe_3O_4 is uniformly dispersed in the epoxy resin matrix, arranged along the direction of the magnetic field. In addition, the orientation of rGO@Fe_3O_4 increases with the magnetic field intensity. After doping 30% (wt) rGO@Fe_3O_4 into epoxy resin and curing under a 500 Gs magnetic field, the rGO@Fe_3O_4/EP composite material is anisotropic and has a higher thermal conductivity (increased by 196.60%) parallel to the direction of the magnetic field compared to a pure ring oxygen resin.

1. Introduction

In recent years, graphene/polymer composite materials have attracted much research interest. Graphene is a two-dimensional material with a honeycomb lattice structure formed by a single layer of carbon atoms through sp^2 hybridization, and its thickness is only 0.335 nm which is the size of one carbon atom.[1,2] Due to its unique microstructure, graphene has many excellent physical properties, such as the highest intrinsic strength (~130 GPa),[3] the highest carrier mobility (up to 200 000 $cm^2\ V^{-1}\ s^{-1}$),[4] and the highest room temperature thermal conductivity (~5000 $W\ m^{-1}\ K^{-1}$, in-plane thermal conductivity), *etc.*[5] Compared with conventional composite materials or pure polymer materials, adding a small amount of graphene often makes the composite material show a huge improvement in mechanical,[6] electrochemical,[7] or thermal properties.[8] At present, there are many studies on graphene composite materials, such as adding graphene to epoxy resin to improve the thermal conductivity of epoxy resin, and adding graphene to metallic copper to improve the thermal conductivity of copper.[9–11] The results show that the thermal conductivity of the composites prepared by adding graphene directly into the matrix does not increase significantly. First of all, the arrangement of graphene in the matrix is extremely inconsistent, and the heat transfer direction along each layer of graphene is inconsistent. In addition, the thermal conductivity of graphene in the vertical laminar direction is only 30–50 $W\ m^{-1}\ K^{-1}$, which is quite different from that in the laminar direction. This characteristic will make the heat mainly transfer between graphene lamellae, thus limiting the overall performance of graphene composites.[12,13] Therefore, the arrangement of graphene in the matrix and the low thermal conductivity in the vertical plane direction must be considered when studying graphene composite materials.[14,15]

Magnetic nanoparticles are composed of transition metal or alloy nanoparticles embedded in nonmetallic media. They have the dual characteristics of magnetic particles and nanomaterials, and have attracted wide attention in basic research and technical applications. By loading magnetic nanoparticles on the surface of graphene to prepare composite materials, it not only inherits the good properties of graphene, but also gives full play to the advantages of magnetic nanomaterials such as superparamagnetism, high catalytic activity and good biocompatibility,[16–18] which makes the materials have application prospects in many aspects. Cakmak *et al.*[19] synthesized rGO–Fe_3O_4–TiO_2 ternary nanocomposites and dispersed them into ethylene glycol to prepare nanofluids. It was found that the rGO–Fe_3O_4–TiO_2/EG nanofluids had stable thermal conductivity at different temperatures and could be used for heat transfer applications. Suo *et al.*[20] studied the sensitivity of the composite Fe_3O_4–GO@SiO_2 for the determination of trace metals in environmental water samples, and the test showed that seven heavy metal ions in different environmental water samples could be determined simultaneously, and the detection limit of the target analyte was within the range of 2.023–13.810 ng L^{-1} under the optimal conditions. Zhang *et al.*[21]

---

[a] *Department of Polymer Science and Engineering, School of Chemical Engineering and Technology, Tianjin University, Tianjin 300350, P. R. China. E-mail: cdyuan@tju.edu.cn*

[b] *Key Laboratory of Mechanism Theory and Equipment Design of Ministry of Education, School of Mechanical Engineering, Tianjin University, Tianjin 300354, China. E-mail: gexiang.hkust@gmail.com*

prepared Fe_3O_4@C/rGO nanocomposite with three-layer structure and studied its microwave absorption performance. The synergistic effect of Fe_3O_4 and carbon materials is beneficial to the composites to obtain good impedance matching characteristics and strong electromagnetic attenuation. The preparation method of magnetic graphene and the selection of magnetic particles are very important to its structure and properties, and the appropriate preparation process should be selected according to the basic properties of the product or the application target. Common synthesis methods include hydrothermal and solvothermal method, chemical graft method, chemical co-precipitation method, microwave-assisted synthesis method, and so on.[22] Barai *et al.*[23] successfully synthesized rGO–Fe_3O_4 nanocomposites through ultrasound-assisted co-precipitation method, and prepared rGO–Fe_3O_4-based nanofluids under the action of ultrasound. When the concentration of rGO–Fe_3O_4 was 0.2 vol%, the thermal conductivity of the nanofluids increased by 83.44% at 40 °C. Sundar *et al.*[24] synthesized rGO–Fe_3O_4–TiO_2 ternary nanocomposites using sol–gel technology, and prepared stable ternary hybrid nanofluids based on ethylene glycol, and studied the effects of various conditions on the physical properties, heat transfer performance and friction coefficient of the nanofluids. Yan *et al.*[25] prepared magnetic GNS–Fe_3O_4 hybrid compounds as filler in epoxy resin by co-precipitation method, which were highly aligned in the epoxy resin through magnetic field action. The results showed that the thermal conductivity of epoxy resin/GNS–Fe_3O_4 composites in parallel magnetic field orientation increased by 139% and 41%, respectively, compared with those of composite epoxy resin with magnetic graphene random distribution and in vertical orientation. After composite with magnetic nanoparticles, graphene is superparamagnetic and can be arranged in the polymer matrix under the action of magnetic field to form an effective heat conduction channel, which is more conducive to the improvement of the thermal conductivity of the matrix.

With the rapid development of science and technology, in certain occasions, higher requirements are put forward for the thermal conductivity of traditional polymer materials. As a commonly used thermosetting resin matrix, epoxy resin has the characteristics of strong bonding ability, excellent electrical insulation, stable chemistry, and low curing shrinkage.[26] However, the epoxy resin will be brittle after cross-linking and curing, with poor heat resistance, impact resistance, and crack resistance.[27] Therefore, graphene is a good candidate to be used as a reinforcing agent to be filled into the epoxy resin system to improve various properties of the epoxy resin for obtaining an epoxy resin-based composite material with excellent comprehensive properties.

Combining the advantages of the above materials, in this study, we synthesized rGO@Fe_3O_4 nanocomposites in one step through a simple solvothermal method, then blended rGO@Fe_3O_4 as a filler with epoxy resin, and cured in an external magnetic field to obtain rGO@Fe_3O_4/EP composite materials. After that, scanning electron microscopy (SEM), X-ray diffraction (XRD), X-ray photoelectron spectroscopy (XPS), Raman, thermal conductivity, and other characterizations were employed to analyze the structure, micro-morphology, and thermal conductivity of the sample.

2. Experimental

2.1 Chemical materials

Flake graphite (325 mesh) was provided by Unigram Carbon Graphene Materials Co., Ltd (Hebei, China; UCGM). Hexahydrate and ferric chloride (AR, ≥99.0%), ethylene glycol (AR), sodium acetate (NaAc, AR, ≥99.0%), tributyl phosphate (AR, 98.5%), sulfuric acid (AR, 95–98%), phosphoric acid (AR, 85%), hydrogen peroxide (30%), potassium permanganate (AR, ≥99.5%) were purchased from Aladdin Chemistry Co. Ltd (Shanghai, China). Polyethylene glycol ($M_w = 2000$) and epoxy resin (E-51) were purchased from Macklin Biochemical Co., Ltd (Shanghai, China). Polyamide resin (V125 resin, curing agent of EP with amino value of 340 mg KOH per g) was purchased from Danbao Resin Co., Ltd (Anhui, China).

2.2 Preparation of rGO@Fe_3O_4 and rGO@Fe_3O_4/EP composites

Graphene oxide (GO) was synthesized from flake graphite by an improved Hummers method.[28] Using the synthesized GO and $FeCl_3 \cdot 6H_2O$ as raw materials, rGO@Fe_3O_4 nanocomposites were prepared by a solvothermal method which can complete the deposition of Fe_3O_4 nanoparticles on graphene sheets while reducing GO. Firstly, 60 mg GO was added to 30 ml of ethylene glycol and dispersed by ultrasonic for 0.5 hours to form a stable GO solution. Then, 1.2 g $FeCl_3 \cdot 6H_2O$, 3.6 g NaAc, and 1 g polyethylene glycol were added into the GO solution in sequence. After that, the solution was stirred for 0.5 hours with ultrasonic vibration. Hence, the chemicals can be fully dissolved faster. The mixed solution was transferred to a polytetrafluoro-ethylene reactor and kept at 200 °C for 12 hours. When the solution was cooled down to room temperature, the resulting product was collected by a magnet adsorption method. Finally, the collected product was thoroughly washed with deionized water and absolute ethanol for several times, dried in a vacuum drying oven at 60 °C for 12 hours, and ground into powder to obtain rGO@Fe_3O_4 nanocomposite materials.

As shown in Fig. 1, the preparation process of the rGO@Fe_3O_4/EP composite is described as follows. Firstly, an appropriate amount of rGO@Fe_3O_4 was weighed according to 5% of the mass of epoxy resin, added into absolute ethanol, and ultrasonically dispersed for 0.5 hours to form a stable dispersion. Then, the rGO@Fe_3O_4/ethanol dispersion was added into the epoxy resin at 80 °C, stirred ultrasonically for 10 minutes, and then heated at 80 °C for 2 hours to remove the solvent. Tributyl phosphate and polyamide resin were added into the above mixed liquid as accelerators. The liquid was stirred evenly and kept in a vacuum oven to remove air bubbles. Finally, the liquid was cured under a specific magnetic field (0 Gs, 100 Gs, 500 Gs), and the curing process were carried out at room temperature for 24 h, at 100 °C for 1 hour, and at 150 °C for 2 hours sequentially.

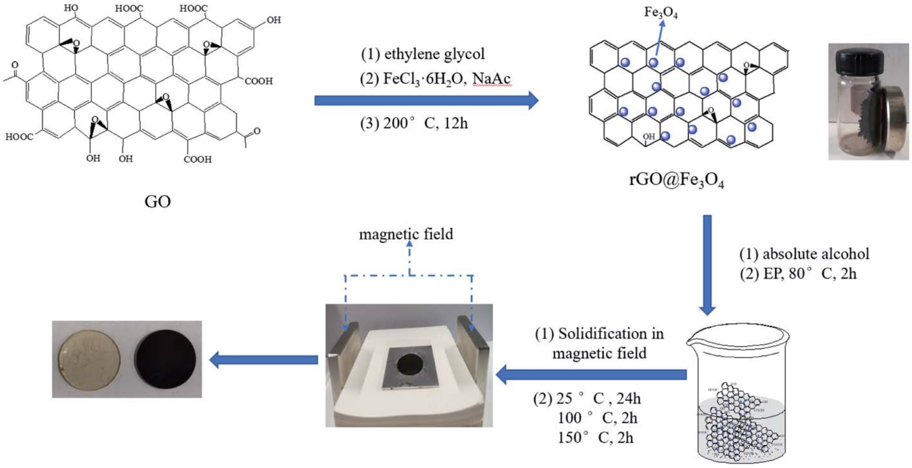

Fig. 1 Synthesis of rGO@Fe_3O_4 and preparation of rGO@Fe_3O_4/EP.

2.3 Characterization

The morphology and microstructure of the GO and rGO@Fe_3O_4 samples were characterized by SEM (Zeiss Merlin Compact, Carl Zeiss AG, Germany). XPS (ESCALAB 250XI, Thermo Fisher Scientific Inc., USA) was used to determine the elemental composition and the functional group information of the samples, in which Al Kα was used as the X-ray source and carbon C 1s as the corrected peak position ($E_{\mathrm{C\ 1s}} = 284.6$ eV). FT-IR (Nicolet 6700, Thermo Fisher Scientific Inc., USA) was used to determine the chemical functional group information of the samples. The measurement range was 500–4000 cm^{-1}, and the resolution was 2 cm^{-1}. The crystal structure of the samples was analyzed by an XRD (Rigaku D/MAX-1200 diffractometer, Tokyo, Japan) operating at 40 kV and 100 mA. The Cu-Kα radiation (wavelength $\lambda = 0.15406$ nm) was employed to obtain the diffraction patterns in a 2θ range of 5°–80° with a scanning speed of 5° min^{-1}. The internal structure of the sample was characterized and analyzed by a DXR Microscope Raman spectrometer (DXR, Thermo Fisher Scientific Inc., Waltham, MA, USA) with a laser wavelength of 532 nm and a scanning range of 100–3500 cm^{-1}.

2.4 Performance test

The magnetic property of the sample was analyzed by a vibrating sample magnetometer (VSM, PPMS-9, Quantum Design Inc., USA). The thermogravimetric analysis (TGA) test was performed using a thermal analyzer (SDT Q600, TA Instruments, USA) from 30 °C to 800 °C with a heating rate of 10 °C min^{-1} under a continuous nitrogen flow. The laser thermal conductivity meter (NETZSCH LFA 467, Germany) was used to measure the in-plane thermal diffusivity. The thermal conductivity (λ) is calculated as follows:

$$\lambda = \alpha \rho c_{\mathrm{p}}$$

where α and ρ are the thermal diffusivity and density of the composite material, which are measured at room temperature; c_{p} is the specific heat of the composite material, which can be measured from −10 °C to 50 °C with a heating rate of 10 °C min^{-1} using a differential thermal scanning calorimeter (DSC Q2000, TA Instruments, USA) by a sapphire method.

3. Results and discussion

3.1 Characterization of GO, rGO, and rGO@Fe_3O_4 nanocomposites

As shown in Fig. 2, the morphology and microstructure of the prepared GO and rGO@Fe_3O_4 nanocomposites can be revealed by the SEM images. In Fig. 2a and b, GO presents a typical corrugated sheet structure with a smooth surface and a thin sheet thickness. In Fig. 2c and d, Fe_3O_4 nanoparticles are uniformly and densely attached to the rGO sheet, acting as a barrier and reducing the force between the rGO sheets.

Raman spectroscopy was used to further characterize the structural characteristics of GO and rGO@Fe_3O_4

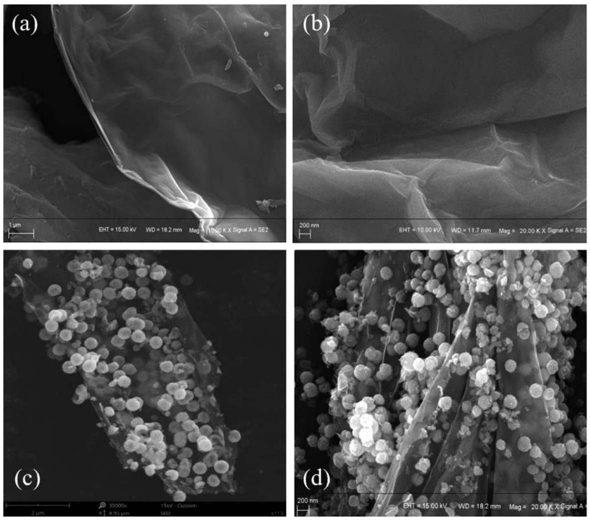

Fig. 2 (a and b) SEM images of GO; (c and d) SEM images of rGO@Fe_3O_4 nanocomposite.

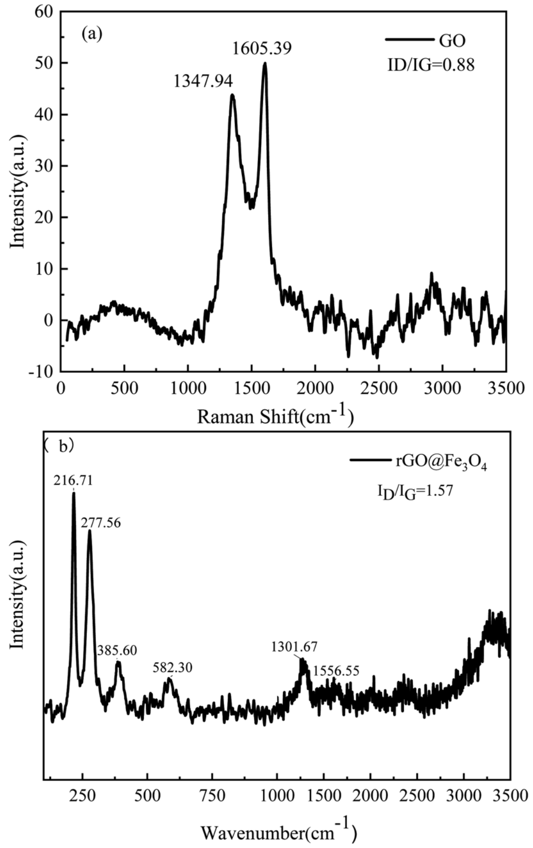

Fig. 3 Raman spectra of GO (a) and rGO@Fe_3O_4 (b).

nanocomposites (Fig. 3a and b). In the Raman spectrum of GO, there are obvious peaks at 1351.80 cm^{-1} and 1607.32 cm^{-1}, corresponding to the D band and G band, respectively. The defects in the structure can be determined by the intensity ratio of I_D to I_G. The I_D/I_G peak intensity ratios of GO and rGO@Fe_3O_4 are 0.88 and 1.57, respectively. Compared with GO, the G band of rGO@Fe_3O_4 is shifted closer to graphene (1580.4 cm^{-1}),[29] indicating that GO was successfully reduced to rGO. In addition, there are peaks at 216.71 cm^{-1}, 277.56 cm^{-1}, 385.60 cm^{-1}, and 582.30 cm^{-1} in the Raman spectrum of rGO@Fe_3O_4 nanocomposites, which are typical peaks of Fe_3O_4.[30] The results of Raman spectroscopy proved that rGO@Fe_3O_4 nanocomposites were successfully synthesized.

Fig. 4 shows the infrared spectra of GO, rGO, Fe_3O_4, and rGO@Fe_3O_4 nanocomposites. The infrared spectrum of GO has obvious characteristic peaks at 3401.82 cm^{-1}, 1743.33 cm^{-1}, 1238.08 cm^{-1}, and 1060.66 cm^{-1}, corresponding to –OH, C═O, C–O, and C–O–C functional groups, respectively. The peak at 1629.55 cm^{-1} is due to the skeleton vibration of aromatic C═C in GO. It shows that there are a lot of oxygen-containing functional groups on the surface of GO. In the infrared spectra of rGO and rGO@Fe_3O_4 nanocomposites, several characteristic peaks of GO are significantly weakened or disappeared, indicating that most of the oxygen-containing groups have been reduced and removed. Compared with rGO, rGO@Fe_3O_4 nanocomposite has a characteristic peak at 563.11 cm^{-1}, which is caused by the stretching vibration of the Fe–O bond. The above-mentioned FTIR analysis shows that the GO in the rGO@Fe_3O_4 nanocomposite has been reduced, and it is confirmed that Fe_3O_4 nanoparticles are present on the reduced graphene sheet.

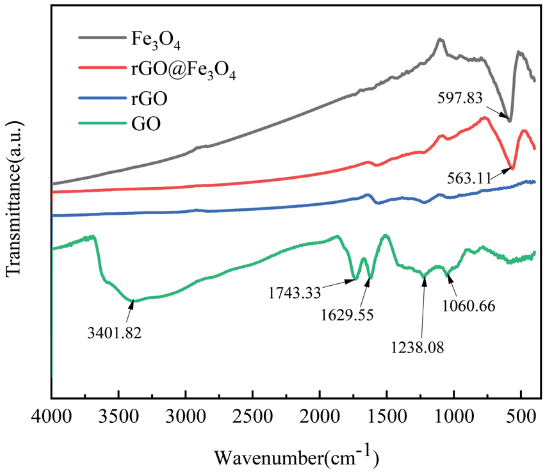

Fig. 4 FTIR spectrum of GO, rGO, Fe_3O_4 and rGO@Fe_3O_4.

XPS technology was used to analyze the chemical composition and functional groups of GO and rGO@Fe_3O_4 nanocomposites. For GO, the C 1s spectrum (Fig. 5b) corresponds to four carbon component peaks with different binding energies: C–C (284.06 eV), C═C (284.57 eV), C–O (285.95 eV), and C═O (288.97 eV), indicating that GO is rich in oxygen functional groups.[31] In the C 1s spectrum of the rGO@Fe_3O_4 nanocomposite (Fig. 5c), the relative intensity of the oxygen-containing functional groups decreases significantly, indicating that GO is effectively deoxidized and reduced to rGO. Fig. 5d shows the Fe 2p spectrum of the composite material, there are two deconvolution peaks at 723.4 eV and 709.8 eV, corresponding to the spin orbit peaks of Fe $2p_{1/2}$ and Fe $2p_{3/2}$ of Fe_3O_4, respectively.[32] It is proved that mixed oxides of Fe(III) and Fe(II) are formed in the composite. There are three split peaks in the O 1s spectrum of the composite material (Fig. 5e), which may be caused by the chemical bonds of different oxygen elements in Fe_3O_4 (O–Fe) and rGO (O–C). The XPS results showed that rGO@Fe_3O_4 nanocomposite was successfully synthesized, and Fe_3O_4 can be combined with rGO well.

Fig. 6a shows the XRD patterns of GO, rGO and rGO@Fe_3O_4 composites. GO has a sharp diffraction peak at $2\theta = 10.6°$, corresponding to the (100) crystal plane of GO. According to the calculation of Bragg equation,[33] the crystal plane spacing is about 0.87 nm. It shows that the carbon structure has lattice distortion, which is mainly because a large number of functional groups are inserted into the graphite lamellar in the oxidation process, which changes the lump structure of the graphite and makes the GO of the single atomic layer stripped off, thus increasing the specific surface area and adsorption site of the material. rGO has a (002) diffraction peak at $2\theta = 23.36°$, and the crystal plane spacing is 0.38 nm, which is much smaller than that of GO. It is due to the reduction of oxygen-containing functional groups and the corresponding reduction of layer spacing after solvothermal reduction of GO. It can be seen from

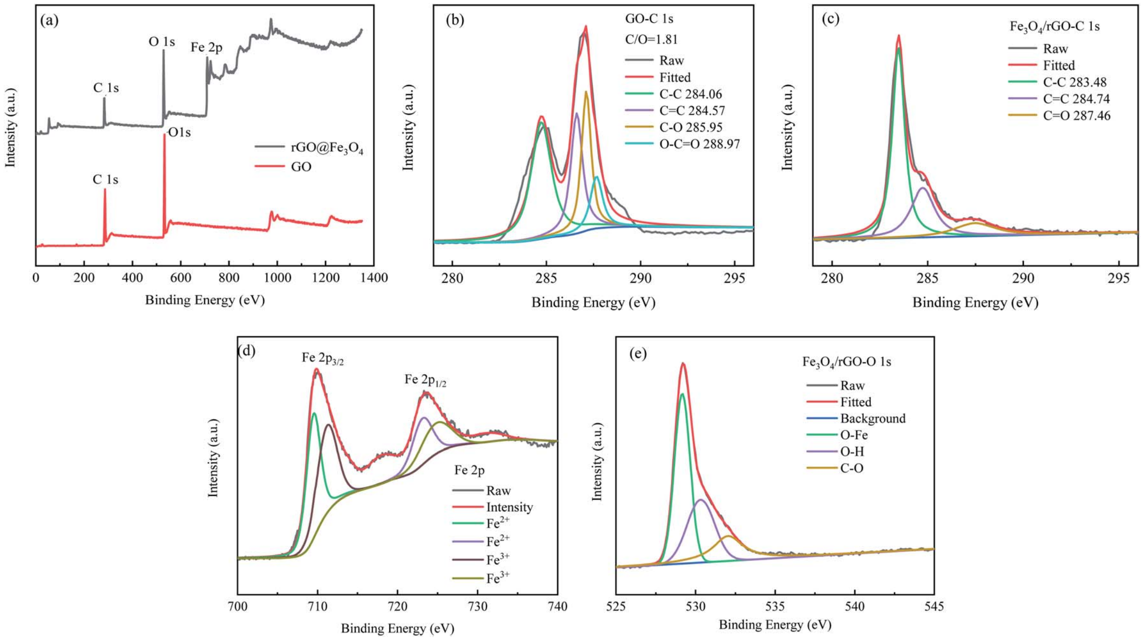

Fig. 5 (a) XPS spectra with survey scan of GO and rGO@Fe_3O_4 nanocomposites; (b and c) C 1s XPS spectra of GO and rGO@Fe_3O_4 nanocomposites, (d and e) Fe 2p XPS spectra of rGO@Fe_3O_4 nanocomposites.

the figure that the main peaks of the XRD spectra of rGO@Fe_3O_4 composites and Fe_3O_4 nanoparticles are in the same position. The diffraction peaks at $2\theta = 18.3°$, $30.14°$, $35.48°$, $43.08°$, $53.54°$, $56.94°$ and $62.64°$ correspond to the crystal planes of (111), (220), (311), (400), (422), (511) and (440), respectively. It is consistent with the standard XRD data of cubic inverse spinel structure of magnetite (JCPDS No. 19-0629),[34,35] indicating the presence of magnetite Fe_3O_4 in the composite material. According to Sherle's formula,[36] the grain size of Fe_3O_4 nanoparticles in rGO@Fe_3O_4 was calculated to be about 71.70 nm. As can be seen from Fig. 6b, the rGO@Fe_3O_4 composite material has a low and broad diffraction peak at $2\theta = 24.22°$, which indicates that GO has become a smaller and thinner rGO, and that the rGO@Fe_3O_4 composite material has been successfully prepared. However, compared with the characteristic peak of pure rGO, the diffraction peak of rGO in rGO@Fe_3O_4 is relatively weak. This is because a large number of Fe_3O_4 nanoparticles are adsorbed on the surface of graphene, which effectively impedes the interlamellar accumulation of graphene and makes it

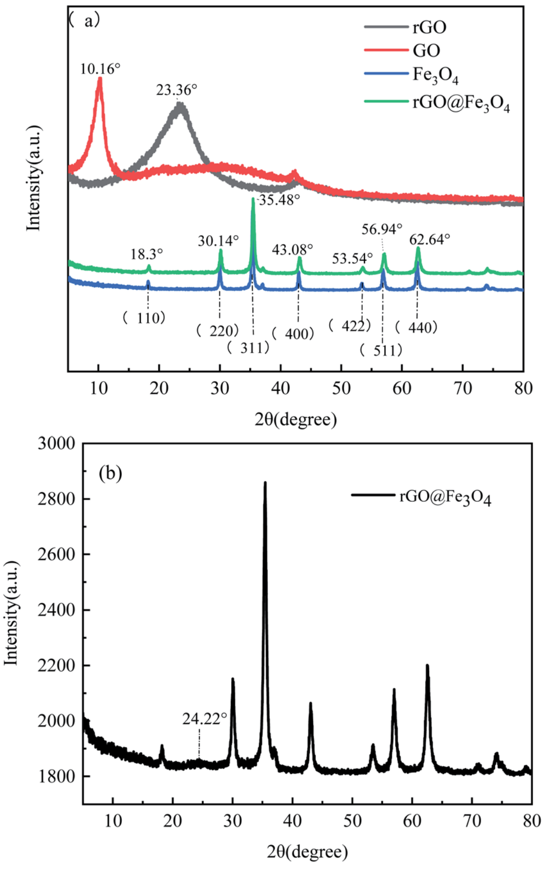

Fig. 6 (a) XRD patterns of GO, rGO, Fe_3O_4 and rGO@Fe_3O_4 composites; (b) magnified XRD pattern of rGO@Fe_3O_4 composites.

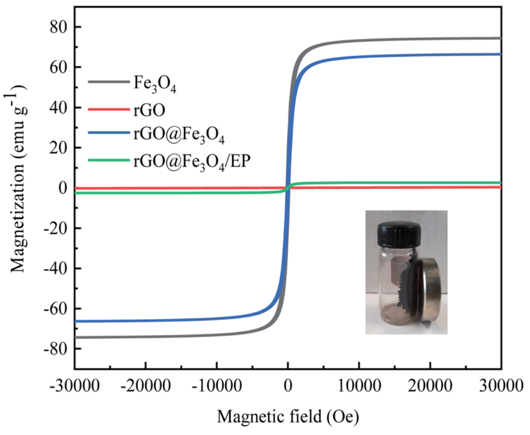

Fig. 7 VSM patterns of rGO, Fe_3O_4, rGO@Fe_3O_4 nanocomposites and rGO@Fe_3O_4/EP composites.

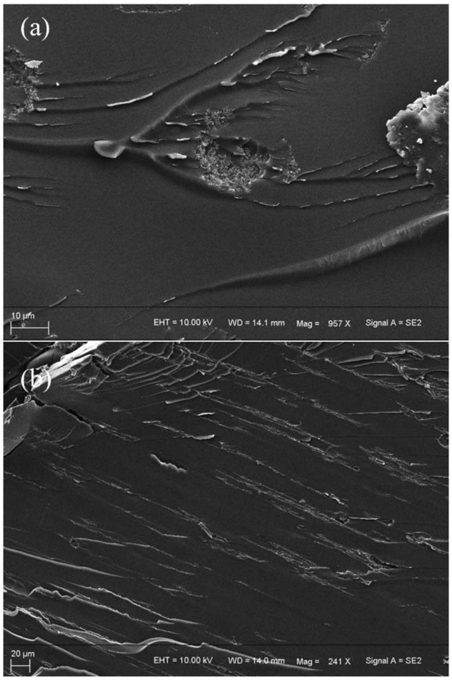

Fig. 8 Cross-sectional SEM image of rGO@Fe_3O_4/EP composite material (a) without magnetic field induction; (b) parallel to the direction of the magnetic field.

difficult to form a graphene-like layered accumulation structure, resulting in an unobtrusive diffraction peak.[37]

The magnetic properties of GO, Fe_3O_4, and rGO@Fe_3O_4 nanocomposites were measured by a vibrating sample magnetometer. The hysteresis loops of Fe_3O_4 and rGO@Fe_3O_4 nanocomposites (Fig. 7) both show an S shape, and there is no obvious coercivity, indicating that both of them have superparamagnetic properties.[38] Although the saturation magnetization of rGO@Fe_3O_4 nanocomposite (66.39 emu g^{-1}) is slightly lower than that of Fe_3O_4 (74.39 emu g^{-1}), there is still enough saturation magnetization to achieve magnetic adsorption. The magnetic saturation intensity of rGO@Fe_3O_4/EP composite is small (2.55 emu g^{-1}), which may be due to the small doping amount of magnetic graphene.

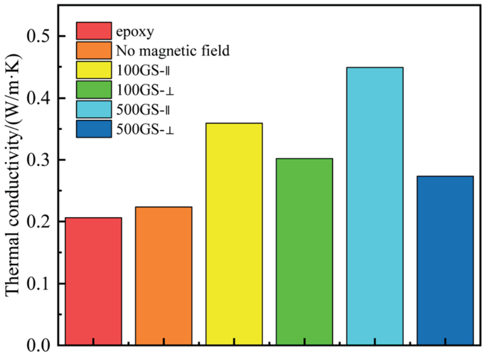

Fig. 9 Thermal conductivity diagram of EP, rGO@Fe_3O_4/EP composite.

Table 1 Thermal conductivity of rGO@Fe_3O_4/EP composites with different rGO@Fe_3O_4 contents and magnetic field

Doping amount of rGO@Fe_3O_4/%	ρ/(g cm^{-3})	C_p/(J g^{-1} K^{-1})	α/(mm^2 s^{-1})	λ/(W m^{-1} K^{-1})
0	—	—	—	0.206
5%	—	—	—	0.224
5% (100 $Gs_{\parallel}$)	1.153	1.882	0.217	0.360
5% (100 $Gs_{\perp}$)	1.133	1.882	0.178	0.302
5% (500 $Gs_{\parallel}$)	0.965	1.882	0.247	0.449
5% (500 $Gs_{\perp}$)	0.950	1.882	0.153	0.274
15% (500 $Gs_{\parallel}$)	0.920	2.322	0.253	0.541
30% (500 $Gs_{\parallel}$)	0.934	2.353	0.278	0.611

3.2 Performance analysis of rGO@Fe_3O_4/EP nanocomposites

Fig. 8 shows the SEM images of the fracture surface of the rGO@Fe_3O_4/epoxy resin composite. After being oriented by a magnetic field, rGO@Fe_3O_4 exhibits an orderly arranged microstructure in the epoxy resin. This microstructure is conducive to the formation of heat transmission paths and the conduction of interface heat.

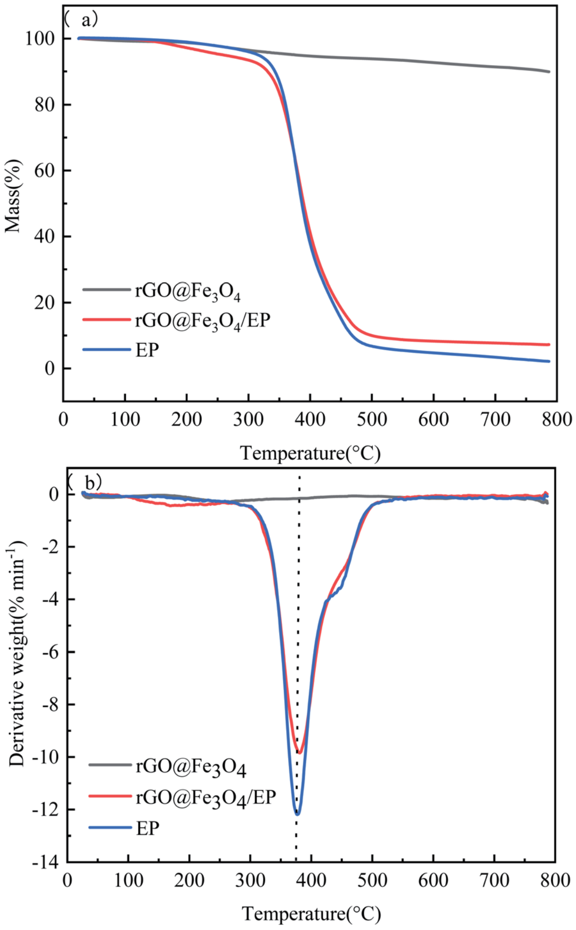

Fig. 10 (a) TG and (b) DTG curves of EP, rGO@Fe_3O_4 nanocomposites, and rGO@Fe_3O_4 composite.

Table 2 The detailed thermal decomposition parameters of EP, rGO@Fe_3O_4 and the composite

Samples	$T_{5\%}$ (°C)	$T_{30\%}$ (°C)	T_{max} (°C)	R_{max} (% min^{-1})	T_{HRI}[a] (°C)	Mass residual at 800 °C (%)
EP	318.83	368.63	374.98	−12.13	170.87	2.17
rGO@Fe_3O_4	360.05	—	—	−0.15	—	90.08
rGO@Fe_3O_4/EP	261.01	370.09	379.95	−9.77	159.96	7.22

[a] The heat-resistance index of the sample is calculated by the following equation: $T_{HRI} = 0.49 \times [T_{5\%} + 0.6 \times (T_{30\%} - T_{5\%})]$.[40–43]

The thermal conductivity of pure epoxy resin and rGO@Fe_3O_4/EP composite materials was measured with a laser thermal conductivity meter. Compared with the pure epoxy resin (0.206 W m^{-1} K^{-1}), the thermal conductivity of the composite (0.224 W m^{-1} K^{-1}) increases by only 8.43% (Fig. 9) when the composite was cured without external magnetic field. After being oriented by an external magnetic field, the composite material exhibits excellent anisotropic thermal conductivity. When oriented under a 100 Gs magnetic field, the thermal conductivity of the in-plane parallel magnetic field direction is 0.360 W m^{-1} K^{-1}. When the magnetic field intensity is 500 Gs, the thermal conductivity of the in-plane parallel magnetic field direction is as high as 0.449 W m^{-1} K^{-1}. It can be seen that the thermal conductivity will increase slightly with increasing the magnetic field. Compared with pure epoxy resin, the thermal conductivity of in-plane parallel magnetic field increases by 117.60% while that of vertical magnetic field (0.274 W m^{-1} K^{-1}) only increases by 33.01% at 500 Gs, which indicates that the composite has anisotropic thermal conductivity. When the magnetic field induces the directional arrangement of rGO@Fe_3O_4 in the epoxy resin matrix, it can form a heat conduction path to facilitate the directional heat transfer, and effectively reduce the phonon scattering and thermal boundary resistance, so that the thermal conductivity along the magnetic field can be greatly improved.[39] It can be seen from Table 1 that the thermal conductivity of rGO@Fe_3O_4/EP composites increases with the increase of rGO@Fe_3O_4 content. When 30% rGO@Fe_3O_4 is doped as filler, the thermal conductivity is as high as 0.611 W m^{-1} K^{-1}, an increase of 196.60% compared with pure epoxy resin.

Fig. 10 shows the thermal performance of EP, rGO@Fe_3O_4, and rGO@Fe_3O_4/EP composites. It can be seen from the TG curves that the mass loss of rGO@Fe_3O_4 is very small, which is mainly attributed to the vaporization of the water absorbed on the surface of the material and part decomposition of carbonaceous materials. The remaining rGO and Fe_3O_4 will not undergo oxidation reaction under the protective effect of nitrogen, and the structure is stable and does not change. Pure epoxy and rGO@Fe_3O_4/EP composites begin to lose weight at about 150 °C, and have been basically completely decompose at 600 °C, the coke rate is 2.17% and 7.22%, respectively. The improvement of coke yield of rGO@Fe_3O_4/EP composites is due to the existence of stable rGO and Fe_3O_4 nanoparticles. Compared with pure epoxy, the T_{max} of rGO@Fe_3O_4/EP composite increases by 5.03 °C, and the maximum mass loss rate (R_{max}) is reduced by 24.16%. In addition, the heat resistance index (T_{HRI}) is often used to evaluate the thermal stability of the cured resin. As can be seen from Table 2, the heat resistance index (159.96 °C) of the rGO@Fe_3O_4/EP composites is slightly lower than that of pure epoxy resin (170.87 °C), which may be due to the enhancement of heat conduction leading to rapid transfer of external heat to the interior. In general, the TGA results show that rGO@Fe_3O_4/EP composites have excellent thermal stability.

4. Conclusions

The magnetic rGO@Fe_3O_4 was prepared in one step by a solvothermal method. Fe_3O_4 nanoparticles were deposited on the surface of rGO to form a synergistic effect, which could make the rGO sheets align along the magnetic field direction. The rGO@Fe_3O_4/EP nanocomposite was prepared by applying an external magnetic field during the curing process. In the epoxy resin matrix, rGO@Fe_3O_4 was arranged in an orderly manner in the direction of the magnetic field, so that the thermal conductivity of the EP nanocomposite in the direction of the magnetic field was significantly enhanced, which made the nanocomposite material show obvious anisotropic thermal conductivity. This work provided some research foundation and application value for improving the thermal conductivity and anisotropy of epoxy resin.

Conflicts of interest

There are no conflicts to declare.

Notes and references

1 R. R. Haering, *Can. J. Phys.*, 1958, **36**, 352–362.

2 X. A. Li, B. L. Wang and Z. R. Liu, *Mater. Rep.*, 2012, **26**, 61–65.

3 C. Lee, X. Wei, J. W. Kysar and J. Hone, *Science*, 2008, **321**, 85–388.

4 S. V. Morozov, K. S. Novoselov, M. I. Katsnelson, F. Schedin, D. C. Elias, J. A. Jaszczak and A. K. Geim, *Phys. Rev. Lett.*, 2007, **100**, 016602.

5 A. A. Balandin, S. Ghosh, W. Bao, I. Calizo, F. Miao and C. N. Lau, *Nano Lett.*, 2008, **8**, 902.

6 D. G. Papageorgiou, I. A. Kinloch and R. J. Young, *Prog. Mater. Sci.*, 2017, **90**, 75–127.

7 D. Verma, P. C. Gope, A. Shandilya and A. Gupta, *Trans. Indian Inst. Met.*, 2014, **67**, 803–816.

8 R. Bauld, W. Choi, P. Bazylewski, R. Divigalpitiya and G. Fanchini, *J. Mater. Chem. C*, 2018, **6**, 2901–2914.
9 J. Kim, B. S. Yim, J. M. Kim and J. Kim, *Microelectron. Reliab.*, 2012, **52**, 595–602.
10 S. H. Song, K. H. Park, B. H. Kim and Y. W. Choi, *Adv. Mater.*, 2013, **25**, 732–737.
11 Y. J. Wan, L. C. Tang, L. X. Gong, Y. B. Li, L. B. Wu, J. X. Jiang and G. Q. Lai, *Carbon*, 2014, **69**, 467–480.
12 L. C. Tang, Y. J. Wan, D. Yan, Y. B. Pei and L. Zhao, *Carbon*, 2013, **60**, 16–27.
13 Y. F. Li, D. Datta, S. Li, Z. Li and V. B. Shenoy, *Comput. Mater. Sci.*, 2014, **93**, 68–73.
14 B. W. Zhang, B. W. Li and C. S. Xie, *Mater. Rep.*, 2007, **21**, 171–178.
15 S. X. Yang, W. C. Jiao, Z. M. Chu and C. W. Zhang, *Fiber Reinf. Plast./Compos.*, 2019, 92–100.
16 A. Akbarzadeh, M. Samiei and S. Davaran, *Nanoscale Res. Lett.*, 2012, **7**, 144.
17 J. E. Lee, B. Tsedenbal, B. H. Koo and S. H. Huh, *Korean J. Mater. Res.*, 2020, **30**, 589–594.
18 E. Rozhina, A. Danilushkina, F. Akhatova, R. Fakhrullin, A. Rozhin and S. Batasheva, *J. Biotechnol.*, 2021, **325**, 25–34.
19 N. K. Cakmak, Z. Said, S. Sundar and A. K. Tiwar, *Powder Technol.*, 2020, **372**, 235–245.
20 L. Z. Suo, X. Y. Dong, X. Gao, J. F. Xu, X. M. Lu and L. S. Zhao, *Microchem. J.*, 2019, **149**, 104039.
21 H. X. Zhang, Z. R. Jia, A. L. Feng, Z. H. Zhou and L. Chen, *Composites, Part B*, 2020, **199**, 108261.
22 R. Greta, Y. Zhou, K. Roman and F. Conrad, *Angew. Chem., Int. Ed.*, 2011, **50**, 826–859.
23 D. P. Barai, B. A. Bhanvase and V. K. Saharan, *Ind. Eng. Chem. Res.*, 2019, **58**, 8349–8369.
24 S. L. Sundar, K. V. V. C. Mouli, Z. Said and A. C. M. Sousa, *J. Therm. Sci. Eng. Appl.*, 2021, **13**, 1–45.
25 H. Y. Yan, Y. X. Tang, W. Long and Y. F. Li, *J. Mater. Sci.*, 2014, **49**, 5256–5264.
26 Y. N. Xie, H. Lei and Q. Shi, *Eng. Plast. Appl.*, 2018, **46**, 143–147.
27 X. B. Hong, K. Xie, Y. Pan and J. Y. Xiao, *Materials Reports*, 2005, **19**, 44–48.
28 E. L. K. Chng and M. Pumera, *Chem.–Eur. J.*, 2013, **19**, 8227–8235.
29 B. Shen, D. Lu, W. Zhai and W. Zhang, *J. Mater. Chem. C*, 2012, **1**, 50–53.
30 H. W. Wang, T. Liang, D. M. Xu, K. Liao, R. Wang and C. J. Yan, *Nanoscale*, 2018, **10**, 17814–17823.
31 J. Chen, B. W. Yao, C. Li and G. Q. Shi, *Carbon*, 2013, **64**, 225–229.
32 B. J. Tan, K. J. Klabunde and P. M. A. Sherwood, *Chem. Mater.*, 2002, **2**, 186–191.
33 H. Cole, *J. Appl. Crystallogr.*, 1970, **3**, 405–406.
34 M. Zong, Y. Huang, Y. Zhao, P. B. Liu, Y. Wang and Q. F. Wang, *Mater. Lett.*, 2013, **106**, 22–25.
35 Y. Yang, M. Li, Y. P. Wu, T. Wang, J. Ding, B. Y. Zong, Z. H. Yang and J. M. Xue, *Nanoscale*, 2016, **8**, 15989–15998.
36 A. L. Patterson, *Phys. Rev.*, 1939, **56**, 978–982.
37 M. Khalaj, A. Sedghi, H. N. Miankushki and S. Z. Golkhatmi, *Energy*, 2019, **188**, 116088.
38 B. J. Li, H. Q. Cao, J. Shao and J. H. Warner, *J. Mater. Chem.*, 2011, **21**, 5069–5075.
39 K. M. F. Shahil and A. A. Balandin, *Nano Lett.*, 2012, **12**, 861–867.
40 R. S. Lehrle and R. J. Williams, *Macromolecules*, 1994, **27**, 3782–3789.
41 J. Deng, X. Q. Liu, C. Li and J. Zhu, *RSC Adv.*, 2015, **5**, 15930–15939.
42 L. Tang, J. Dang, M. K. He and J. Y. Li, *Compos. Sci. Technol.*, 2018, **169**, 120–126.
43 Y. Tang, W. C. Dong, L. Tang, Y. K. Zhang, J. Kong and J. W. Gu, *Compos. Commun.*, 2018, **8**, 36–41.